PAPER

Anodization of large area Ti: a versatile material for caffeine photodegradation and hydrogen production†

Marcel Sihor, [iD] ‡[ab] Muhammad Bilal Hanif, [iD] ‡[a]
Guru Karthikeyan Thirunavukkarasu, [iD] [a] Viktoriia Liapun,[a]
Miroslava Filip Edelmannova,[b] Tomáš Roch,[c] Leonid Satrapinskyy,[c] Tomas Plecenik,[c]
Sajid Rauf,[d] Karol Hensel,[e] Olivier Monfort [iD] [a] and Martin Motola [iD] *[a]

Facile, single-step, and scalable fabrication of large-area (*i.e.*, ~20 cm^2) TiO$_2$ nanostructures (TNS) with excellent photocatalytic activity under UVA light was carried out *via* electrochemical anodization. Anodization in a glycerol-based electrolyte containing fluoride ions was conducted at applied potentials of 20–80 V (20 V per step) for 100 min. Anodization at 20 V (TNS-20) and 40 V (TNS-40) led to formation of nanotubular TiO$_2$, whereas, at 60 V (TNS-60) and 80 V (TNS-80) porous TiO$_2$ was obtained. The highest caffeine photodegradation rate was obtained using TNS-20 (rate constant; k = 0.0069 min^{-1}) and TNS-60 (rate constant; k = 0.0067 min^{-1}). Moreover, hydrogen production by decomposition of methanol on large-area anodized Ti is reported here for the first time. The highest hydrogen production rate was observed using TNS-20 (production rate of ~6200 ppm, *i.e.*, 25.83 ppm min^{-1}), followed by TNS-60 (production rate of ~5900 ppm, *i.e.*, 24.58 ppm min^{-1}). The efficiency of these two materials is due to the interplay of the structure, morphology, and HO$^{\bullet}$ radical generation that favor TNS-20 and TNS-60 for both photocatalysis and hydrogen production. This work shows a potential strategy to synthesize large-area anodic TNS efficient for photocatalysis and hydrogen production. Synthesis of large-area materials is crucial for most real (photo)electrochemical applications where TNS of several cm^2 in macroscopic surface area are necessary.

1. Introduction

TiO$_2$ has gained considerable attention ever since the pioneering work of Fujishima and Honda in 1972 (ref. 1) on the use of TiO$_2$ as a catalyst for water splitting under UV light. Due to its exceptional physicochemical properties, TiO$_2$ is

[a] *Department of Inorganic Chemistry, Faculty of Natural Sciences, Comenius University in Bratislava, Ilkovicova 6, 842 15 Bratislava, Slovakia. E-mail: martin.motola@uniba.sk*
[b] *Institute of Environmental Technology, CEET, VSB-Technical University of Ostrava, 17. listopadu 15/2172, 708 00, Ostrava-Poruba, Czech Republic*
[c] *Department of Experimental Physics, Faculty of Mathematics, Physics, and Informatics, Comenius University in Bratislava, 842 48 Bratislava, Slovakia*
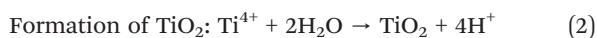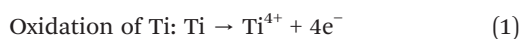[d] *College of Electronics and Information Engineering, Shenzhen University, Guangdong Province, 518000, China*
[e] *Division of Environmental Physics, Faculty of Mathematics, Physics, and Informatics, Comenius University in Bratislava, 842 48 Bratislava, Slovakia*
† Electronic supplementary information (ESI) available: Photographs of TiO$_2$ nanostructures; schematic representation of a home-made photoreactor; photograph of the bed reactor; AFM data summarized in a table; comparison table of our materials *vs.* other reports. See DOI: https://doi.org/10.1039/d2cy00593j
‡ These authors contributed equally to this work.

nowadays used in a plethora of (photo)electrochemical applications[2,3] including photocatalysis, solar cells, and water splitting. For the majority of these applications, a high specific surface area is advantageous, thus, nanostructured TiO$_2$ is often used in the form of nanotubes[4] or the frequently used commercially available nanoparticles. In particular, anodic TiO$_2$ nanotube (TNT) layers offer a high surface-to-volume ratio.[5] The synthesis of TNT layers *via* electrochemical anodic oxidation was first reported in 1984.[6] The advantage of TNT layers compared to nanotubes prepared *via* different techniques (*e.g.*, hydrothermal, electrospinning), as well as compared to nanoparticles or nanofibers, is their direct growth on the Ti substrate in a suitable electrolyte.[7] This leads to good electrical connection and strong mechanical adhesion between the nanotubes and the underlying Ti substrate without the necessity of any further immobilization. Such TNT layers are highly ordered and uni-directional shaped as their known sister material – porous alumina.[8] Compared to the non-ordered TiO$_2$ nanostructures, TNT layers show improved charge carrier separation and transport that stems from the vectorial charge carrier transport along the nanotube walls[9] which is responsible for enhanced

This journal is © The Royal Society of Chemistry 2022

Catal. Sci. Technol., 2022, **12**, 5045–5052 | **5045**

performance in (photo)electrochemical applications including photocatalysis in both liquid and gas phases.[10–12]

Despite the great number of reports published in the last two decades regarding the synthesis and application of anodic TNT layers, only a few reports can be found on the synthesis of TNT layers on a scale larger than a few cm^2.[10,13–19] This relates to specific synthesis challenges that occur when a potential is applied to larger Ti substrates during anodization, e.g., when larger areas are anodized, the absolute current flowing between the Ti working electrode and the counter electrode is much higher than that for smaller areas. This leads to an increase in the electrolyte temperature and leads to the so-called dielectric breakdown.[17] A new electrolyte composition and a possible efficient cooling system will be necessary for the synthesis of TNT layers with a large area of several cm^2 with properly adjustable dimensions. Indeed, electrolytes based on viscous organic compounds (e.g., glycerol, ethylene glycol) containing small amounts of distilled H_2O and NH_4F are promising for the synthesis of large area TNT layers.[10,17] On the other hand, by anodization of Ti (besides TNTs) porous TiO_2 can be formed. The mechanism involved in field-assisted dissolution supported by fluoride ions (so called from top to bottom) is as follows (eqn (1)–(3)).

$$\text{Oxidation of Ti: Ti} \rightarrow \text{Ti}^{4+} + 4e^- \tag{1}$$

$$\text{Formation of TiO}_2\text{: Ti}^{4+} + 2H_2O \rightarrow TiO_2 + 4H^+ \tag{2}$$

$$\text{Dissolution of TiO}_2\text{: TiO}_2 + 6F^- + 4H^+ \rightarrow [\text{TiF}_6]^{-2} + 2H_2O \tag{3}$$

There is a thin line for the change of the morphology between the nanotubes and nanostructures (porous ones) during anodization. Indeed, the potential- and current-induced dissolution of the formed TNTs in the presence of fluoride ions is well known,[20,21] i.e., the formed TNTs are destroyed, and a rather porous structure is formed. Although the porous TiO_2 is often overlooked in the literature as it is considered as "unsuccessful synthesis" of TNT layers, the formed porous TiO_2 possesses a high specific surface area and a sufficient number of active sites that are crucial for (photo)electrochemical applications. Therefore, it is of high interest to study also the formed porous TiO_2 during anodization, not only the TNTs. The preparation of large area TiO_2 nanostructures (TNS) is crucial as for most real-life (photo)electrochemical applications (e.g., photocatalytic air and water cleaners or hydrogen production on a big scale) materials of several cm^2 in macroscopic surface area are necessary. There are several reports that show the photocatalytic activity of TNS (in particular nanotubes) prepared via anodization of large area Ti (>1 cm^2);[13–19] however, to the best of our knowledge, there is no report on hydrogen production.

In the present study, an accelerated synthesis approach is reported for the synthesis of large-scale (e.g., ~20 cm^2) TNS. Both TNT layers and porous TiO_2 were prepared via

anodization in an organic-based electrolyte containing fluoride ions. TiO_2 shows characteristic solar absorption and significantly higher photocatalytic activities to produce hydrogen from methanol under sunlight and aid in photo-oxidization of organic pollutants in wastewater. TNS were characterized using relevant techniques to ensure the crystallographic information, electronic transitions (absorption), and morphology through X-ray diffractometry (XRD), UV-visible spectroscopy, and scanning electron microscopy (SEM), respectively. In addition, caffeine was employed as a model organic pollutant to ensure the photocatalytic activity of the prepared TNS. Thus, the present work highlights a remarkable mechanism to synthesize TNS applicable to practical photocatalytic activities.

2. Experimental section

2.1 Synthesis of TNS

Titanium foil (TF, Sigma-Aldrich, 99.7% purity, 5 × 5 cm^2 square with 0.127 mm thickness) was utilized as a precursor substrate for the growth of TNS. A circle of 5 cm in diameter was drawn on the square (TF) and cut out into three corners to make a "drop" shape which was used as the working electrode. A similarly shaped TF was used as the counter electrode. One corner was utilized as a handle to fasten the electrode. The distance between the electrodes was kept at 1.6 cm. Therefore, the reaction area for the formation of TNS was approx. 20 cm^2. Electrochemical anodization was performed from 20 to 80 V (20 V per step) for 100 min in a glycerol-based electrolyte (Central-Chem, Slovakia), containing 270 mM NH_4F in 100 mL glycerol and 100 mL distilled H_2O. The anodization was performed in a 250 mL glass beaker. To avoid overheating of the electrolyte, cooling with an ice bath was conducted to achieve a constant temperature of the electrolyte during the anodization – 8 °C. During the whole experiment, the current varied during the anodization process (Table S1†), and the electrolyte was kept under stirring using a magnetic stirrer. The current was adjusted to I_{MAX} = 5 A with a variable voltage range of 20–80 V (20 V per step), respectively, and the following abbreviations were used for the anodically prepared materials TNS-20, TNS-40, TNS-60, and TNS-80, respectively, as shown in Fig. S1† along with TF (not anodized). After anodization, the as-prepared TNS were immersed for 5 min in isopropyl alcohol (IPA) to remove the adsorbed electrolyte from the surface of TNS. Subsequently annealing was conducted in a muffler furnace at 400 °C for 1 h in an air atmosphere (2.21 °C min^{-1}). Fig. 1 shows the schematic illustration of TNS and their degradation in a caffeine environment along with the photocatalytic conversion of methanol (CH_3OH) to hydrogen (H_2), respectively.

2.2 Materials characterization

The grazing incidence mode was operated in an X-ray diffractometer (XRD, PANalytical, Cu Kα radiation, λ = 1.5418
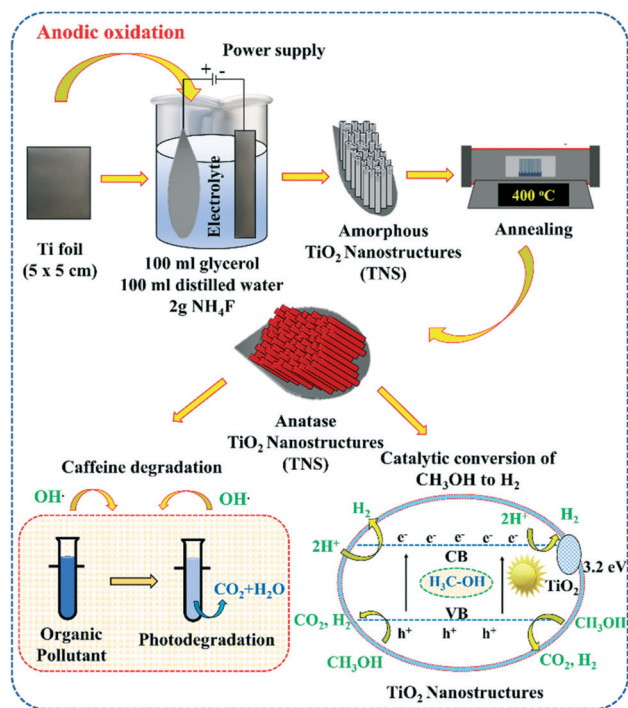
Fig. 1 Schematic illustration of the fabrication of large area TNS (approx. 20 cm^2) and the mechanism of caffeine degradation and H_2 production.

Å) to study the crystal structure of TNS. The morphology was acquired through a scanning electron microscope (SEM, Lyra 3 Tescan, at 10 kV). To obtain deeper insight into the influence of surface roughness and skewness of the different TNS, atomic force microscopy was conducted (AFM, NT-MDT NTegra Aura) in semi-contact tapping mode using standard silicon AFM probes (NT-MDT, HA-NC ETALON series). UV-vis diffuse reflectance spectra (DRS) were obtained using a Shimadzu UV-2600 spectrometer (Shimadzu, Japan), equipped with an integrating sphere 2600 Plus.

Photogeneration of hydroxyl radicals (HO$^•$) was determined *via* a fluorescence spectrophotometer (RF-6000, Shimadzu). Detection of HO$^•$ was performed in a solution containing TNS using coumarin as a probe molecule (0.5 mM). In the presence of HO$^•$, coumarin formed a fluorescent compound (hydroxycoumarin) which was detected at λ_{em} = 456 nm (λ_{ex} = 325 nm). Standard curves were plotted with known concentrations of hydroxycoumarin (+99%, Alfa Aesar) to quantify the amount of generated HO$^•$ under UVA irradiation.

2.3 Photodegradation of caffeine

Photocatalytic degradation of caffeine was carried out in a self-constructed photocatalytic reactor.[22] This reactor consisted of a flat-bottomed glass bowl with a volume of 80 ml which was placed on a magnetic stirrer. A low cylinder of titanium mesh was placed vertically in the center around the magnetic stirrer to serve as a support for materials. The

titanium mesh was chosen for its strength, inertness, and also porosity so that the entire volume of liquid can be mixed during the reaction due to the stirrer inside as shown in Fig. S2.† The materials were placed on the pedestal and 50 ml of a 20 ppm aqueous caffeine solution (ReagentPluss, Sigma-Aldrich) was poured into the assembled apparatus. The titanium nanotube plate was kept at a sufficient height at all times to allow sufficient circulation of the solution around the entire surface due to agitation. The entire assembly was placed in the dark for 30 min to eliminate the effect of sorption early in the reaction. Afterwards, the system was placed on a magnetic pad sampled (time = 0 min) and irradiation began. A halogen lamp (metal–halogen arc-lamp, HQI TS-OSRAM 400 W/D6500K with a UVB pyrex filter) with a maximum intensity of 0.73 mW cm^{-2} in the 365 nm (230–350 nm) region was used as the radiation source. From the system, 0.3 ml of solution was withdrawn using a micropipette at regular intervals (20 min) for 2 h. The collected solutions were kept in the dark and then diluted with 0.5 ml of distilled water. The concentration of caffeine was evaluated from the absorbance *via* UV spectroscopy (Jasco V530).[23,24] To investigate the stability of the samples, the photocatalytic measurements were performed 3 times. Generally, the differences between the repeated measurements did not exceed ±5%.

2.4 Hydrogen production

Hydrogen production was carried out in a stainless-steel batch photoreactor (volume 305 ml, Fig. S3†). The batch, comprised of 100 ml of 50% methanol and our material, was bubbled with helium (He) for 30 minutes before the reaction started (*i.e.*, light irradiation), after which the reactor was gas sealed. An 8 W mercury (Hg) lamp with maximum intensity at 254 nm (Ultra-Violet Products Inc.) was chosen as the radiation source and was placed vertically in a quartz tube passing through the reactor. The reaction mixture was irradiated for 4 h and gas was collected with a septum gas syringe at 0, 1, 2, 3, and 4 h, respectively. The gas was immediately analyzed after collecting using a gas chromatograph (Shimadzu Tracera GC-2010Plus) equipped with a BID (barrier ionization detector). The hydrogen production measurements were performed 3 times for each sample to ensure the stability of the materials. Generally, the differences between the repeated measurements did not exceed ±5%.

3. Results and discussion

3.1 Synthesis, structure, and morphology

Anodization of large area (20 cm^2) Ti was conducted in a glycerol-based electrolyte to obtain the here presented material. There are various adjustable parameters during anodization (*e.g.*, applied potential, current, temperature) that affect the resulting materials' morphology.[25–27] In this report, constant temperature using different applied potentials was studied. As discussed later in this work, our

This journal is © The Royal Society of Chemistry 2022

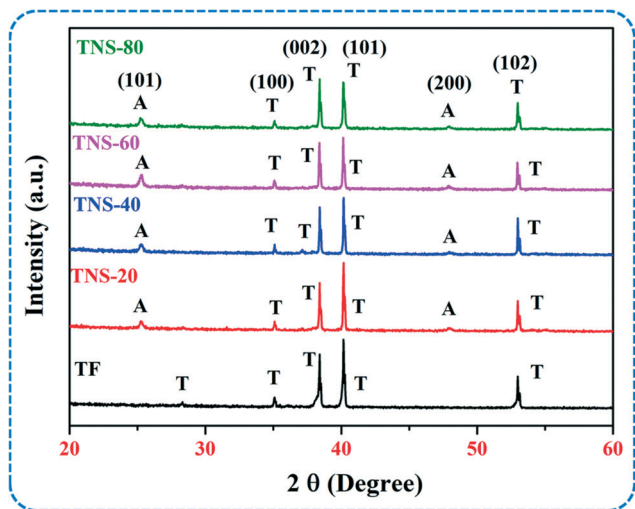*Catal. Sci. Technol.*, 2022, **12**, 5045–5052 | **5047**

Fig. 2 X-ray diffraction patterns of different TNS (TF, TNS-20, TNS-40, TNS-60, and TNS-80, respectively). The diffractions labeled A and T are assigned to TiO_2 anatase and titanium, respectively.

anodization conditions led to the formation of TNT layers and also porous TiO_2 – to avoid any confusion, we named the prepared materials as TNS.

Fig. 2 shows the XRD patterns of annealed TNS prepared at different potentials (20 V, 40 V, 60 V, and 80 V, labelled TNS-20, TNS-40, TNS-60, and TNS-80, respectively) along with annealed TF (used as a reference material). Two different crystalline structures were detected in all NSs: i) tetragonal anatase TiO_2 ($P4_2/mmm$; ICCD 01-086-1157)[4,28] and ii) hexagonal metallic Ti ($P6_3/mmc$; ICCD 00-044-1294) that stemmed from the underlying Ti substrate.[29,30] In the case of TF, only the metallic Ti was identified although a thin layer (a few tens of nanometers) of TiO_2 anatase was certainly present as TF was annealed similarly to TNS. However, it was not detected by XRD.

Representative SEM images of the annealed TF and TNS are shown in Fig. 3. Anodically prepared TNS are 1.5–2.5 μm thick. Annealed TF (Fig. 3a) possesses a typical surface morphology of an initial Ti substrate.[31] For the sample anodized at 20 V (TNS-20), a nanotubular morphology was observed (Fig. 3b and f) with an inner diameter of the tubes of approx. 50 nm and a layer thickness of approx. 1.5 μm. By anodization at 40 V (TNS-40, Fig. 3c and g), a nanotubular structure was observed (cross-section Fig. 3g); however, the surface of the tubes was destroyed (Fig. 3c) due to the voltage/current induced dissolution of the formed tubes in the presence of fluoride ions.[20,21] Thus the mechanical stability of the tubes was disturbed and as a result a rupture of the tube mouth was observed.[4,32] Approx. 1.7 μm thick layers were formed in TNS-40. Anodization at 60 V (TNS-60, approx. 1.7 μm thick; Fig. 3d and h) and 80 V (TNS-80, approx. 2.5 μm thick; Fig. 3e and i) led to the formation of porous TiO_2. The complete distortion of the nanotubular structure and formation of a porous one are due to increased applied potential (thus increased current) that led to this outcome. Nevertheless, the porous TiO_2 shows similar adhesion to the underlying Ti substrate and overall mechanical stability to the nanotubular structure, *i.e.*, the formed layers do not peel off the substrate.

Additional information about the surface morphology alterations of TF and TNS was acquired by AFM (Fig. 4). The relevant nanoscale roughness was determined on the area of 10×10 μm^2. Although the AFM scans of the used area (100 μm^2) cannot be considered as an entirely whole-surface representative, such AFM analysis is beneficial to study the proceeding changes (*i.e.*, roughness) in the different TiO_2 materials (TF and TNS in this work). Complete data obtained by AFM are summarized in the ESI† (Table S2). The surface of TF (Fig. 4a) shows cracks with typical widths of tens/ hundreds of nanometers minimizing the stress induced by the welding production processes of the Ti substrates
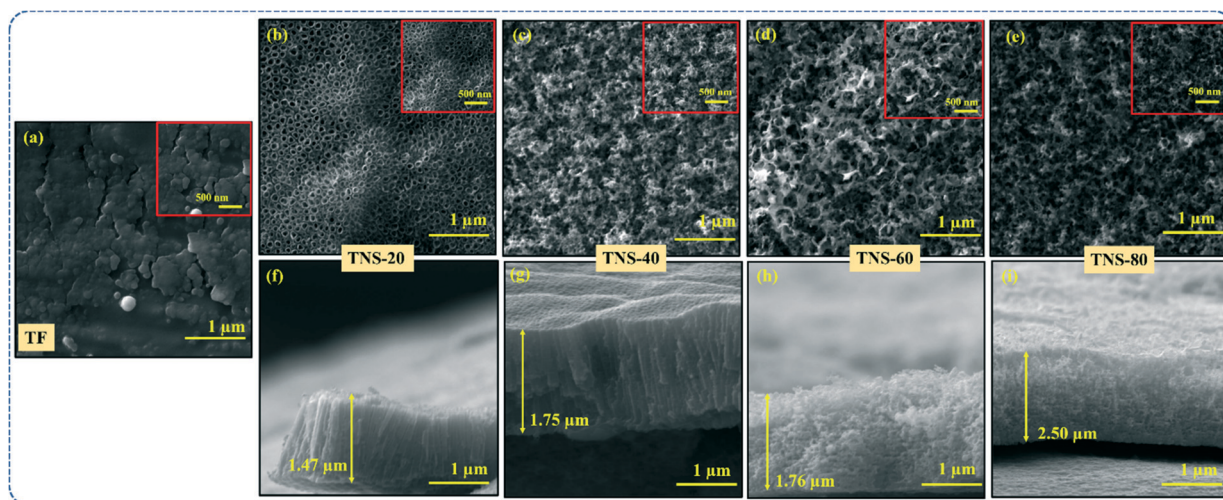

Fig. 3 Representative top and cross-sectional SEM images of different TNS: (a) TF, (b and f) TNS-20, (c and g) TNS-40, (d and h) TNS-60, and (e and i) TNS-80 along with the insets of top view at higher magnification of the corresponding material.

5048 | *Catal. Sci. Technol.*, 2022, **12**, 5045–5052
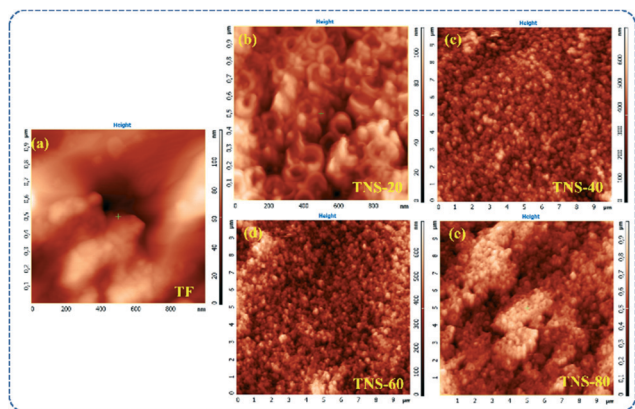
This journal is © The Royal Society of Chemistry 2022

Fig. 4 AFM topography images of different TNS: (a) TF, (b) TNS-20, (c) TNS-40, (d) TNS-60, and (e) TNS-80, respectively.

(commercially available TF). An absolute root mean square (RMS, S_q in nm) value of ~56 nm was obtained for TF. After anodization at 20 V (TNS-20, Fig. 4b), the RMS value increased to S_q ~ 92 nm. This is due to the formation of the nanotubular structure which intrinsically increases the surface roughness of TiO_2.[30] A sudden decrease to S_q ~ 78 nm was observed in TNS-40 due to the following reason. Although TNS-40 possesses a nanotubular structure (Fig. 3e), the surface of the layers is disrupted due to the potential/current induced etching of tubes in the presence of fluoride ions.[20,21] Therefore a decrease in S_q was observed in TNS-40 compared to that in TNS-20. In the case of TNS-60 and TNS-80, after the full collapse of the tubes and formation of porous TiO_2, an increase to S_q ~ 102 nm and S_q ~ 150 nm was determined, respectively. Hence, the roughness of the porous TiO_2 is increased compared to that of nanotubular TiO_2 prepared *via* anodization. Finally, the optical properties of TNS were measured by UV-vis DRS. The optical bandgap (E_g) of TNS-20, TNS-40, TNS-60, and TNS-80, respectively, was determined from the UV-vis DRS spectra (Fig. S4a†) using the Tauc's plot (Fig. S4b†) for indirect transition. The E_g was calculated to be between approx. 3.1 eV to 3.2 eV for all TNS. This is in agreement with previous reports on anodic TiO_2 nanostructures.[33–35]

3.2 Photodegradation of caffeine

TF and TNS were explored for the photocatalytic degradation of caffeine under UVA light irradiation. Fig. 5a and S5† show the corresponding photocatalytic degradation rates and degradation of caffeine. The highest degradation rate was obtained using TNS-20 and TNS-60 which showed similar efficiency. The photocatalytic degradation of caffeine follows the first-order reaction.[36,37] Thus its kinetics can be expressed from the linear variation of $\ln C/C_0$ (C_0 and C is the initial and after the time concentration, respectively) as a function of time (t). The obtained photodegradation rates indicate that both materials prepared *via* anodization, *i.e.*, nanotubular TiO_2 (TNS-20, $k = 0.0069$ min^{-1}) and porous TiO_2
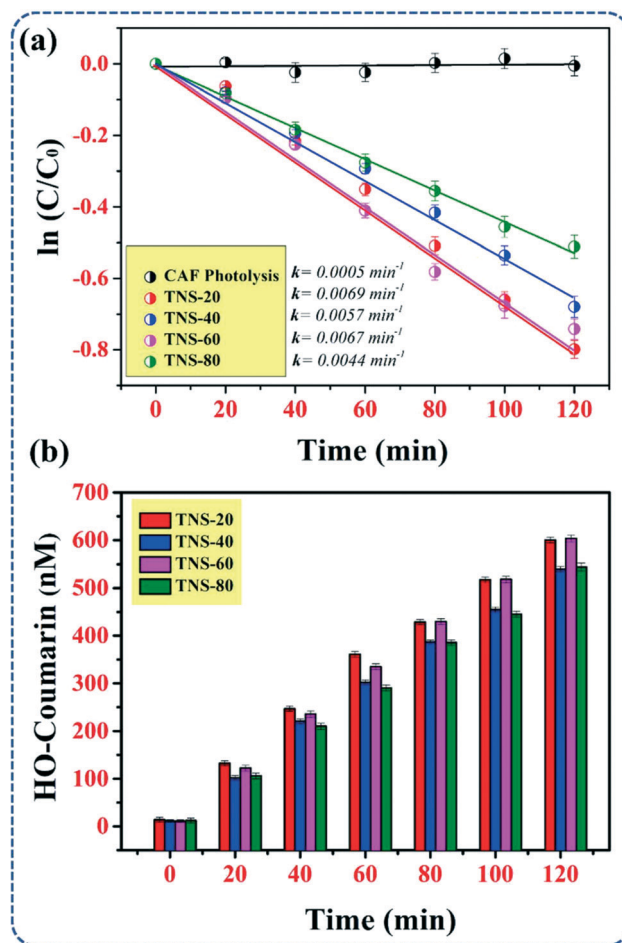

Fig. 5 (a) Photodegradation of caffeine and (b) formation of HO˙ radicals by coumarin assay using different TNS (TNS-20, TNS-40, TNS-60, and TNS-80, respectively).

(TNS-60, $k = 0.0067$ min^{-1}), show an increased degradation rate of caffeine compared to TNS-40 ($k = 0.0057$ min^{-1}) and TNS-80 ($k = 0.0044$ min^{-1}). Not surprisingly, nanotubular TiO_2 showed an efficient photodegradation rate of caffeine which is in good agreement with previous reports on photocatalytic activity of nanotubular TiO_2 layers.[2,3,38] For sample TNS-20, the total organic carbon analysis (performed using TOC-L, Shimadzu) showed a mineralization extent of about 7% after 2 h irradiation which is a satisfactory value for such a short irradiation time. However, a similar photodegradation rate was also obtained using porous TiO_2 (TNS-60). Indeed, although the original nanotubular morphology is lost due to anodization conditions, the formed porous TiO_2 layers possess a highly porous structure that provides enough active sites for caffeine to adsorb and subsequently degrade the pollutant. A decrease in the photodegradation efficiency was observed using TNS-40 and TNS-80, respectively, and the reasons are described as follows. In the case of TNS-40, although a nanotubular morphology is present, the top of the tubes is disturbed. Thus, the overall surface area is decreased compared to that of TNS-20. Indeed, the decrease in the number of active

This journal is © The Royal Society of Chemistry 2022

Catal. Sci. Technol., 2022, **12**, 5045–5052 | **5049**

surface sites of TNS-40 that adsorb caffeine resulted in lower photodegradation efficiency. On the other hand, a full collapse/distortion of tubes was present in TNS-80 and a rather porous structure was formed. Compared to TNS-60, the pores are denser thus providing fewer active sites for caffeine to be adsorbed, *i.e.*, the photodegradation efficiency decreased. The clear difference in the density of the pores is visible on the cross-sectional SEM images for TNS-60 (Fig. 3h) and TNS-80 (Fig. 3i). As the photodegradation of caffeine proceeds at the material/pollutant interface, porosity (or specific surface area) is a crucial factor. Both SEM (Fig. 3) and AFM (Fig. 4) confirmed the presented statements. Here, the Brunauer–Emmett–Teller (BET) theory[39] is not applicable as it is challenging to measure BET on our samples, *i.e.*, to remove the layers from the underlying substrate and proceed with BET measurements. Although it is possible to remove the nanotubular structure from the underlying substrate as reported previously,[40,41] the porous structure shows improved adhesion to the substrate compared to the nanotubular one, thus removing the porous structure, without completely destroying it, is highly challenging and was not successfully conducted yet. Nevertheless, to support our bold explanation statements regarding the photodegradation efficiency of our materials, HO$^{\bullet}$ radical production was conducted (Fig. 5b). Indeed, the amount of generated HO$^{\bullet}$ radicals is another crucial factor for a material to possess efficient photodegradation properties. Generation of HO$^{\bullet}$ radicals proceeds at the materials' interface induced by the incident light irradiation and depends on the materials' surface area, *i.e.*, on the number of active sites. The amount of generated HO$^{\bullet}$ radicals gives an insight into the surface area, although indirectly. Here, enhanced generation of HO$^{\bullet}$ radicals was observed in TNS-20 and TNS-60 compared to TNS-40 and TNS-80. Considering all the presented data, *i.e.*, XRD (Fig. 2), SEM (Fig. 3), AFM (Fig. 4), and HO$^{\bullet}$ radical generation (Fig. 5b) which support each other, the reason for the increased photodegradation efficiency of TNS-20 and TNS-60 is unambiguous. The interplay of the structure, morphology, and HO$^{\bullet}$ radical generation is in favor of the photodegradation efficiency of the herein presented TNS-20 and TNS-60 more than those of TNS-40 and TNS-80. Additionally, photocurrent transients of TNS were recorded in the wavelength range from 300 nm to 420 nm and the results are summarized in the ESI† (Text S1 and Fig. S6). Typical photocurrent transients for TiO$_2$ were obtained with a pronounced increase in photocurrent at λ = 350 nm.[42,43] The obtained photocurrent trends correlate with the obtained photocatalytic results and HO$^{\bullet}$ radical generation.

3.3 Hydrogen production

Hydrogen production (by decomposition of methanol) using TNS was conducted to determine the efficiency of the presented materials. Methanol in a water/alcohol mixture acts as a hole scavenger and undergoes irreversible oxidation.[44–46] As reported,[44–46] the methanol decomposition
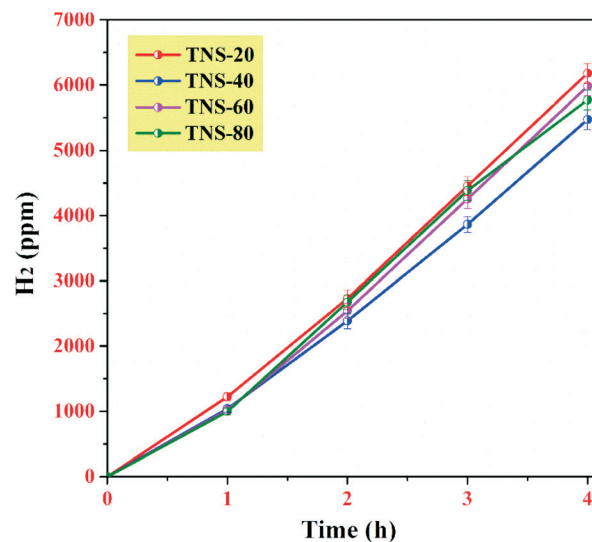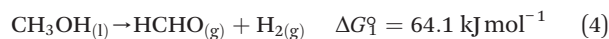

Fig. 6 Time dependence of hydrogen yields during photocatalytic decomposition of methanol in the presence of the investigated photocatalysts.
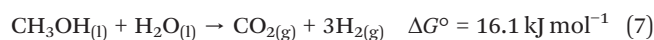
reactions are as follows:

$$CH_3OH_{(l)} \rightarrow HCHO_{(g)} + H_{2(g)} \quad \Delta G_1^{\circ} = 64.1 \text{ kJ mol}^{-1} \quad (4)$$

$$HCHO_{(g)} + H_2O_{(l)} \rightarrow HCO_2H_{(l)} + H_{2(g)} \quad (5)$$
$$\Delta G_2^{\circ} = 47.8 \text{ kJ mol}^{-1}$$

$$HCO_2H_{(l)} \rightarrow CO_{2(g)} + H_{2(g)} \quad \Delta G_3^{\circ} = -95.8 \text{ kJ mol}^{-1} \quad (6)$$

With the overall reaction being:

$$CH_3OH_{(l)} + H_2O_{(l)} \rightarrow CO_{2(g)} + 3H_{2(g)} \quad \Delta G^{\circ} = 16.1 \text{ kJ mol}^{-1} \quad (7)$$

The H$_2$ production rate is summarized in Fig. 6, *i.e.*, the dependence of the H$_2$ yield (in ppm) *vs.* the irradiation time. The highest H$_2$ production was obtained using TNS-20 (approx. 6200 ppm) followed by TNS-60 (approx. 5900 ppm), TNS-80 (approx. 5700 ppm), and TNS-40 (approx. 5500 ppm). Two crucial factors affect the hydrogen production rate: i) the amount of generated HO$^{\bullet}$ radicals and ii) the number of active sites. Indeed, the photoinduced methanol decomposition proceeds at the TNS/methanol interface. Thus, a large specific surface area is necessary for efficient hydrogen production. Moreover, as methanol is primarily decomposed by HO$^{\bullet}$ radicals, the amount of generated radicals is also a significant parameter. Based on the here presented data (Fig. 3–5), the above two crucial factors are intrinsic for TNS-20 and TNS-60. The hydrogen production was also present (and was efficient) for TNS-40 and TNS-80, although their photocatalytic activity (Fig. 5a) was decreased compared to that of TNS-20 and TNS-60. Indeed, the adsorption properties of a material significantly affect the overall (photo)efficiency of the material. Methanol is a substantially smaller molecule than caffeine, thus its

5050 | *Catal. Sci. Technol.,* 2022, **12**, 5045–5052

This journal is © The Royal Society of Chemistry 2022

adsorption on the TNS surface is enhanced compared to caffeine – and is similar in all TNS. As all TNS generate a great amount of HO$^{\bullet}$ radicals (Fig. 5b), the hydrogen production rate is efficient for all TNS.

We somehow tried to compare our obtained results in photocatalysis and hydrogen production of large-area anodized Ti to other reports (summarized in ESI,† Table S3). However, it is tricky to conclude due to the following factors: i) not all reports show rate constants for photocatalytic measurements, ii) the concentration and nature of a studied organic pollutant differ (the majority of reports show results for organic dyes which are not suitable for photocatalytic measurements),[47] iii) the total anodized Ti area differs (from 10 cm^2 to 50 cm^2), and iv) there is a lack of information on the conditions used during the measurements, *i.e.*, intensity of the used light source, wavelength, *etc.* As for hydrogen production, to the best of our knowledge, there is no report on the hydrogen production rate on large-area anodized TNS. Thus, we could not compare it at all as we show such results for the very first time. All in all, the herein presented large-area anodic TNS show an efficient photodegradation rate of caffeine and hydrogen production rate.

Conclusions

In this work, electrochemical anodization of Ti was performed by applying potentials from 20 V to 80 V for 100 min in a glycerol-based electrolyte containing fluoride ions to obtain large area TNS ($\sim$20 cm^2), *i.e.*, nanotubular TiO$_2$ and porous TiO$_2$. The prepared TNS were annealed at 400 °C to obtain crystalline TiO$_2$ anatase. The thickness of the obtained TNS was in the range from 1.5 to 2.5 μm. The surface roughness of TNS increased with increasing applied potential from $S_q \sim 55$ nm to $S_q \sim 150$ nm. The highest caffeine photodegradation extent was obtained using nanotubular TiO$_2$ anodized at 20 V (TNS-20, $k = 0.0069$ min^{-1}) and porous TiO$_2$ (TNS-60, $k = 0.0067$ min^{-1}). The highest hydrogen production rate was obtained using TNS-20 (approx. 6200 ppm, *i.e.*, 25.83 ppm min^{-1}) and TNS-60 (approx. 5900 ppm, *i.e.*, 24.58 ppm min^{-1}). To summarize, we have shown a potential strategy to prepare large-area TNS *via* anodization for real (photo)electrochemical applications including photocatalytic degradation of aqueous pollutants and hydrogen production. We present novel aspects for the development of large surface area TiO$_2$ nanostructure layers prepared by anodization, since macroscopic surface area is necessary for scale-up to industrial applications.

Author contributions

Marcel Sihor: writing, investigation, visualization, methodology, review, editing. Muhammad Bilal Hanif: investigation, writing, methodology, review, editing. Guru Karthikeyan Thirunavukkarasu: investigation, methodology, review. Viktoriia Liapun: investigation, methodology, review. Miroslava Filip Edelmannova: investigation, methodology.

Tomáš Roch: investigation, methodology. Leonid Satrapinskyy: investigation, methodology. Tomas Pleceník: investigation, methodology. Sajid Rauf: methodology, review. Karol Hensel: review, investigation, methodology. Olivier Monfort: review, editing, visualization. Martin Motola: supervision, conceptualization, writing, review, editing, visualization.

Conflicts of interest

There are no conflicts to declare.

Acknowledgements

Notes and references

1   A. Fujishima and K. Honda, *Nature*, 1972, **238**, 37–38.
2   K. Lee, A. Mazare and P. Schmuki, *Chem. Rev.*, 2014, **114**, 9385–9454.
3   S. Shen, J. Chen, M. Wang, X. Sheng, X. Chen, X. Feng and S. S. Mao, *Prog. Mater. Sci.*, 2018, **98**, 299–385.
4   M. Motola, L. Hromadko, J. Prikryl, H. Sopha, M. Krbal and J. M. Macak, *Electrochim. Acta*, 2020, **352**, 136479.
5   R. Beranek, H. Tsuchiya, T. Sugishima, J. M. Macak, L. Taveira, S. Fujimoto, H. Kisch and P. Schmuki, *Appl. Phys. Lett.*, 2005, **87**, 243114.
6   M. Assefpour-Dezfuly, C. Vlachos and E. H. Andrews, *J. Mater. Sci.*, 1984, **19**, 3626–3639.
7   J. M. Macak, H. Tsuchiya, L. Taveira, S. Aldabergerova, P. Schmuki, S. Aldabergerova, P. Schmuki, A. Friedrich and H. Hildebrand, *Angew. Chem., Int. Ed.*, 2005, **44**, 7463–7465.
8   H. Masuda and K. Fukuda, *Science*, 1995, **268**, 1466–1468.
9   J. M. Macak, S. P. Albu and P. Schmuki, *Phys. Status Solidi RRL*, 2007, **1**, 181–183.
10   M. Motola, L. Satrapinskyy, T. Roch, J. Šubrt, J. Kupčík, M. Klementová, M. Jakubičková, F. Peterka and G. Plesch, *Catal. Today*, 2017, **287**, 59–64.

11 M. Motola, M. Baudys, R. Zazpe, M. Krbal, J. Michalička, J. Rodriguez-Pereira, D. Pavliňák, J. Přikryl, L. Hromádko, H. Sopha, J. Krýsa and J. M. Macak, *Nanoscale*, 2019, **11**, 23126–23131.

12 J. M. Macak, M. Zlamal, J. Krysa and P. Schmuki, *Small*, 2007, **3**, 300–304.

13 E. Mena, M. J. Martín de Vidales, S. Mesones and J. Marugán, *Catal. Today*, 2018, **313**, 33–39.

14 C. Xiang, L. Sun, Y. Wang, G. Wang, X. Zhao and S. Zhang, *J. Phys. Chem. C*, 2017, **121**, 15448–15455.

15 J. P. Ghosh, G. Achari and C. H. Langford, *Water Environ. Res.*, 2016, **88**, 785–791.

16 H. Il Kim, D. Kim, W. Kim, Y. C. Ha, S. J. Sim, S. Kim and W. Choi, *Appl. Catal., A*, 2016, 174–181.

17 H. Sopha, M. Baudys, M. Krbal, R. Zazpe, J. Prikryl, J. Krysa and J. M. Macak, *Electrochem. Commun.*, 2018, **97**, 91–95.

18 S. Franz, D. Perego, O. Marchese and M. Bestetti, *J. Water Chem. Technol.*, 2015, **37**, 108–115.

19 M. Szkoda, K. Trzciński, Z. Zarach, D. Roda, M. Łapiński and A. P. Nowak, *Materials*, 2021, **14**, 5686.

20 W. Zhang, Y. Liu, F. Guo, J. Liu and F. Yang, *J. Mater. Chem. C*, 2019, **7**, 14098–14108.

21 K. Indira, U. K. Mudali, T. Nishimura and N. Rajendran, *J. Bio- Tribo-Corros.*, 2015, **1**, 1–22.

22 R. Michal, E. Dworniczek, M. Čaplovičová, M. Gregor, L. Čaplovič, A. Seniuk, P. Kuš and G. Plesch, *Ceram. Int.*, 2014, **40**, 5745–5756.

23 S. A. Bhawani, S. S. Fong and M. N. M. Ibrahim, *Int. J. Anal. Chem.*, 2015, **2015**, 1–8.

24 A. Belay, K. Ture, M. Redi and A. Asfaw, *Food Chem.*, 2008, **108**, 310–315.

25 D. Wang, Y. Liu, B. Yu, F. Zhou and W. Liu, *Chem. Mater.*, 2009, **21**, 1198–1206.

26 J. M. Macak, B. G. Gong, M. Hueppe and P. Schmuki, *Adv. Mater.*, 2007, **19**, 3027–3031.

27 C. W. Lai and S. Sreekantan, *Int. J. Photoenergy*, 2012, **2012**, 1–12.

28 H. Zhang and J. F. Banfield, *J. Mater. Res.*, 2011, **15**, 437–448.

29 M. Motola, L. Satrapinskyy, M. Čaplovicová, T. Roch, M. Gregor, B. Grančič, J. Greguš, Ľ. Čaplovič and G. Plesch, *Appl. Surf. Sci.*, 2018, **434**, 1257–1265.

30 M. Motola, E. Dworniczek, L. Satrapinskyy, G. Chodaczek, J. Grzesiak, M. Gregor, T. Plecenik, J. Nowicka and G. Plesch, *Chem. Pap.*, 2019, **73**, 1163–1172.

31 M. Motola, J. Capek, R. Zazpe, J. Bacova, L. Hromádko, L. Bruckova, S. Ng, J. Handl, Z. Spotz, P. Knotek, K. Baishya, P. Majtnerova, J. Prikryl, H. Sopha, T. Rousar and J. M. Macak, *ACS Appl. Bio Mater.*, 2020, **3**, 6447–6456.

32 O. K. Varghese, D. Gong, M. Paulose, C. A. Grimes and E. C. Dickey, *J. Mater. Res.*, 2003, **18**, 156–165.

33 G. Cha, P. Schmuki and M. Altomare, *Chem. - Asian J.*, 2016, **11**, 789–797.

34 N. Pishkar, Z. Jedi-soltanabadi and M. Ghoranneviss, *Results Phys.*, 2018, **10**, 466–468.

35 H. Fraoucene, V. A. Sugiawati, D. Hatem, M. S. Belkaid, F. Vacandio, M. Eyraud, M. Pasquinelli and T. Djenizian, *Front. Chem.*, 2019, **7**, 66.

36 G. K. Thirunavukkarasu, O. Monfort, M. Motola, M. Motlochová, M. Gregor, T. Roch, M. Čaplovicová, A. Y. Lavrikova, K. Hensel, V. Brezová, M. Jerigová, J. Šubrt and G. Plesch, *New J. Chem.*, 2021, **45**, 4174–4184.

37 G. K. Thirunavukkarasu, J. Bacova, O. Monfort, E. Dworniczek, E. Paluch, M. B. Hanif, S. Rauf, M. Motlochova, J. Capek, K. Hensel, G. Plesch, G. Chodaczek, T. Rousar and M. Motola, *Appl. Surf. Sci.*, 2022, **579**, 152145.

38 M. Zlamal, J. M. Macak, P. Schmuki and J. Krýsa, *Electrochem. Commun.*, 2007, **9**, 2822–2826.

39 S. Brunauer, P. H. Emmett and E. Teller, *J. Am. Chem. Soc.*, 2002, **60**, 309–319.

40 D. Beketova, M. Motola, H. Sopha, J. Michalicka, V. Cicmancova, F. Dvorak, L. Hromadko, B. Frumarova, M. Stoica and J. M. Macak, *ACS Appl. Nano Mater.*, 2020, **3**, 1553–1563.

41 H. Michalkova, Z. Skubalova, H. Sopha, V. Strmiska, B. Tesarova, S. Dostalova, P. Svec, L. Hromadko, M. Motola, J. M. Macak, V. Adam and Z. Heger, *J. Hazard. Mater.*, 2020, **388**, 122054.

42 A. Matsuda, S. Sreekantan and W. Krengvirat, *J. Asian Ceram. Soc.*, 2018, **1**, 203–219.

43 M. Krbal, J. Kucharik, H. Sopha, H. Nemec and J. M. Macak, *Phys. Status Solidi RRL*, 2016, **10**, 691–695.

44 W. C. Lin, W. D. Yang, I. L. Huang, T. S. Wu and Z. J. Chung, *Energy Fuels*, 2009, **23**, 2192–2196.

45 T. Kawai and T. Sakata, *J. Chem. Soc., Chem. Commun.*, 1980, 694–695.

46 J. Chen, D. F. Ollis, W. H. Rulkens and H. Bruning, *Water Res.*, 1999, **33**, 669–676.

47 N. Barbero and D. Vione, *Environ. Sci. Technol.*, 2016, **50**, 2130–2131.